communications materials

A Nature Portfolio journal

Article

https://doi.org/10.1038/s43246-026-01266-y

Spin and orbital excitations in undoped infinite-layer superconducting $PrNiO_2$ and insulating $CaCuO_2$

Check for updates

F. Rosa [1,12] ✉, H. Sahib [2,13], G. Merzoni [1,3], L. Martinelli [1,14], R. Arpaia [4,5], N. B. Brookes [6], D. Di Castro[7,8], K. Wohlfeld [9], M. Zinouyeva [1], M. Salluzzo [10], D. Preziosi [2] & G. Ghiringhelli [1,11] ✉

Infinite-layer nickelates are among the most promising cuprate-akin superconductors, although relevant differences from copper oxides have been reported. Here, we present momentum- and polarization-resolved RIXS measurements on nominally undoped, superconducting $PrNiO_2$, and compare its magnetic and orbital excitations with those of the reference infinite layer cuprate $CaCuO_2$. In $PrNiO_2$, the in-plane magnetic exchange integrals are smaller than in $CaCuO_2$, whereas the out-of-plane values are similar, indicating that both materials support three-dimensional antiferromagnetic correlations. Orbital excitations, associated to the transitions within 3*d* states of the metal, are well reproduced within a single-ion model and display similar characteristics, except the Ni-d_{xy} peak that, besides lying at significantly lower energy, shows an opposite dispersion to that of Cu-d_{xy}. We attribute this difference to the values of the orbital superexchange coupling between nearest neighbor sites. Our observations suggest that infinite-layer cuprates and nickelates share most of the spin and orbital properties, but in nickelates the larger charge-transfer energy Δ and smaller hopping integrals imply smaller spin-fluctuation energy and stronger localization of the doping charge on the metal site.
https://doi.org/10.15151/ESRF-ES-1430231833.

The quest for high-T_c superconductivity has brought to the attention of the condensed matter community the wide family of strongly correlated materials[1–3]. Infinite-layer (IL) nickelates recently gained strong interest[4–11] thanks to their apparent analogies with cuprates, including a square lattice-based structure dominated by superexchange antiferromagnetic interaction[12,13] and the emergence of superconductivity upon hole doping. So far, the latter has been observed only in thin films[14–18], which makes it difficult to assess the magnetic structure of the IL nickelate system, as no direct correspondence with the bulk can be established. The bulk is mostly characterized by the absence of long-range order and the presence of a spin-glass behavior[13,19,20]. Conversely, evidence of spin-spin correlations was reported from extensive Resonant Inelastic X-ray Scattering (RIXS)[12,21], as well as X-ray Magnetic Circular Dichroism (XMCD)[22] experiments in superconducting and non-superconducting thin films.

On the other hand, the analogies between cuprates and IL nickelates[6,23] are not yet sufficient to prove the existence of a single underlying mechanism for unconventional superconductivity[7,24,25], but rather urge further investigation. At the root of the observed affinities is the common $3d^9$ electronic configuration of Cu^{2+} and Ni^{1+} ions occupying the corners of a planar spin 1/2 square lattice, with oxygen ligands along the edges.

Within the Zaanen-Sawatzky-Allen framework[26], earlier works[4,8,11,21,27] tended to regard IL nickelates as genuine Mott-Hubbard insulators, where the ligand-to-metal charge-transfer energy Δ is larger than the Coulomb repulsion *U*, in contrast with charge-transfer insulators (like cuprates),

[1]Dipartimento di Fisica, Politecnico di Milano, Milano, Italy. [2]CNRS, IPCMS UMR 7504, Université de Strasbourg, Strasbourg, France. [3]European XFEL, Schenefeld, Germany. [4]Department of Molecular Sciences and Nanosystems, Ca' Foscari University of Venice, Venice, Italy. [5]Quantum Device Physics Laboratory, Department of Microtechnology and Nanoscience, Chalmers University of Technology, Göteborg, Sweden. [6]ESRF, The European Synchrotron, Grenoble, France. [7]Dipartimento di Ingegneria Civile e Ingegneria Informatica, Università di Roma Tor Vergata, Roma, Italy. [8]CNR-SPIN, Università di Roma Tor Vergata, Roma, Italy. [9]Institute of Theoretical Physics, Faculty of Physics, University of Warsaw, Warsaw, Poland. [10]CNR-SPIN, Complesso Monte Sant'Angelo-Via Cinthia, Napoli, Italy. [11]CNR-SPIN, Dipartimento di Fisica, Politecnico di Milano, Milano, Italy. [12]Present address: II. Physikalisches Institut, Universität zu Köln, Zülpicher Strasse 77, Cologne, Germanyrosa@ph2.uni-koeln.de. [13]Present address: Department of Physics, College of Science, University of Halabja, Halabja, Iraq. [14]Present address: Physik-Institut, Universität Zürich, Zürich, Switzerland. ✉e-mail: francesco1.rosa@polimi.it; giacomo.ghiringhelli@polimi.it

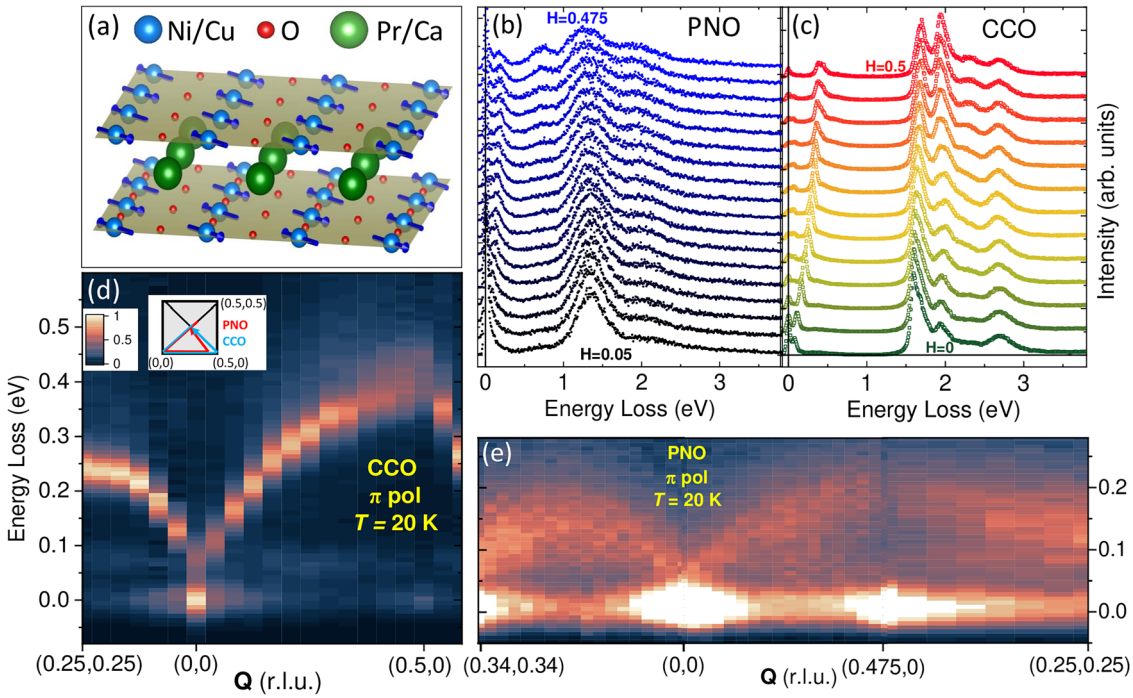


Fig. 1 | Comparison of RIXS spectra on PNO and CCO. a Infinite-layer structure (ocher planes) of PNO (CCO), showing the local tetragonal coordination of the nickel (copper) atoms to the surrounding oxygens; the dark blue arrows on metal sites depict antiferromagnetic spin order (only reported for CCO). **b**, **c** RIXS spectra stacks for PNO and CCO, respectively, along the [*H*, 0] cut of the Brillouin zone. Momentum-dependent RIXS maps of CCO (**d**) and PNO (**e**) along the triple paths of the Brillouin zone, shown in the (**d**) inset for the two samples. All (**d**, **e**) spectra have been normalized to the *dd* energy integral along the interval (1; 3.5) eV.

where $\Delta < U$. A more recent interpretation, originating from RIXS studies on bi- and tri-layer nickelates[28–30], supports a different picture, revealing a mixed charge-transfer/Mott-Hubbard character that may extend to infinite-layer compounds, with Δ not much larger than U. This is consistent with the comparable magnitude of the magnetic exchange interaction in cuprates and nickelates, sensitively depending on Δ ($J \propto 1/\Delta^3$[31]). In both scenarios, the oxygen 2*p* states lie at lower energy than in cuprates, and doped holes are expected to have a stronger metal character, although the precise degree of hybridization remains under debate. Moreover, the role of rare-earth 5*d* states has been proposed to generate Fermi-surface pockets[11,17,24,32] and enable self-doping even in nominally undoped compounds[8,33–35], but recent angle-resolved photoemission measurements have not found clear evidence of such features at the Γ point[36,37].

As for magnetic properties, spin fluctuations are considered to play a major role in the formation of Cooper pairs in cuprates[38,39], and a coexistence of magnetism and superconductivity has been suggested by XMCD[22], as well as muon spin rotation/relaxation in cuprates and IL nickelates[40,41]: therefore, a comparative investigation by other methods is timely.

Here, we used RIXS to investigate the dynamical spin response of the nominally undoped though superconducting IL nickelate $PrNiO_2$ (PNO)[42] and compare it to that of $CaCuO_2$ (CCO)[43,44], which has a similar crystalline structure but fully insulating properties. Despite self-doping and superconductivity, in PNO, the spin excitation peak is sharp and disperses similarly to CCO. We find that the in-plane exchange integrals are smaller in PNO than in CCO, consistently with previous reports[12], while the out-of-plane values are comparable. Polarization-resolved RIXS reveals a better agreement of the PNO orbital excitations (*dds*) with single-ion cross-section calculations, while in CCO, a fourth peak occurs, whose origin remains unclear. Interestingly, the d_{xy} peak displays an opposite dispersion in the two materials, which we interpret as a consequence of distinct orbital superexchange couplings driving the orbiton propagation in the two materials: nearest neighbor for the nickelate, next-nearest neighbor for the cuprate[45].

Results and discussion

Figure 1 displays an overview of RIXS spectra for both samples, showcasing orbital and spin excitations. The common infinite-layer structure is depicted in Panel (a), which can represent either CCO or PNO depending on the assignment of Cu/Ni and Ca/Pr atoms. The antiferromagnetic spin lattice, also shown, has so far been reported only for the cuprate. Panels (b, c) report spectra taken at different transferred momenta along the [*H*,0] cut of the 2D reciprocal space. The orbital (*dd*) excitations at high energy range (1–3 eV) show a small but significant dispersion as a function of the in-plane momentum, as discussed below[45,46]. For the nickelate, an additional feature is observed at 0.7 eV. This excitation has already been reported in the literature[21,47,48] and becomes progressively enhanced towards the Brillouin zone edge. Its out-of-plane character is further supported by the fact that it is more enhanced for π-polarized incident light than σ (see also Fig. 4 below). This feature has mainly been interpreted[11] in terms of hybridization between Ni 3*d* and rare-earth 5*d* states. Here we adopt this interpretation, although alternative scenarios cannot be ruled out. Indeed, a possible extrinsic origin is supported by the fact that the peak appears stronger in samples showing a more intense diffraction signal from impurity phases[49]. The sharp feature dispersing up to ~200 meV in PNO and ~400 meV in CCO is assigned to $\Delta S = 1$ spin excitations, in agreement with previous RIXS work[12,50–55]. These spin excitations follow a single-magnon dispersion across most of the reciprocal space along the M-Γ-X path (panels d, e). Whereas the sharpness of the magnetic peak in CCO is a direct consequence of the long-range antiferromagnetic (AFM) order of the undoped compound [55,56], the coexistence of superconductivity and sharp spin excitations in IL nickelates demonstrates the mild effect of self-doping on magnetism. This constitutes an important difference with respect to cuprates, where the chemical hole doping, required for superconductivity, quickly disrupts spin order and progressively smears the magnon excitation peak[54] across the superconducting dome (see below for a more quantitative comparison). Our observations are consistent with the muon spin rotation measurements in superconducting IL nickelates by Fowlie et al.[41], which hint at a similar

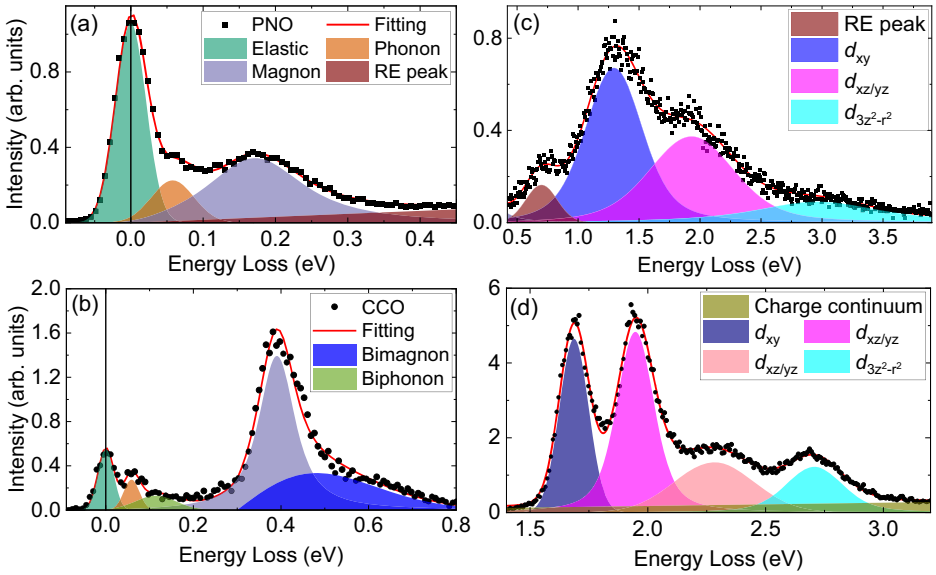


Fig. 2 | Analysis of RIXS spectra. a Fitting of the PNO spectrum with π incident polarization, as described in the main text. Data points were obtained as the sum of different spectra along $[H, 0]$ with H between 0.4 and 0.475 r.l.u. at incident energy 852.48 eV. **b** Same fit for CCO, with $H = 0.465$ r.l.u.; a second Gaussian is added here (light green) representing the phonon overtone, while the rare-earth peak tail has been replaced by the bimagnon continuum (dark blue). Elastic, phonon and magnon colors are the same as in (**a**). **c**, **d** Same fittings as (**a**, **b**) respectively, but focusing on the orbital excitations area.

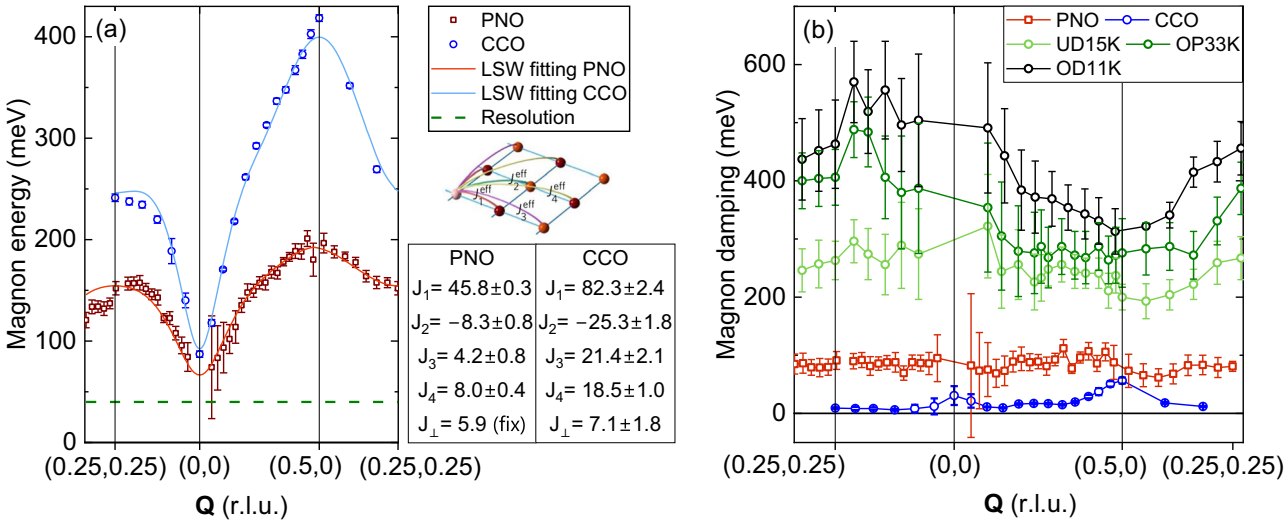


Fig. 3 | Comparison of magnon energy and damping. a Fitting of dispersions of PNO and CCO with the Linear Spin Wave model fit. The definitions and values (in meV) of the four in-plane exchange coupling constants are displayed on the right[53]. **b** Comparison of the damping coefficients of PNO and CCO with those extracted from analogous fittings on Bi2201 cuprate at different doping levels in ref. 54 (UD underdoped, OP optimally doped, OD overdoped). Error bars in both panels represent 95% confidence intervals from the fittings.

coexistence. A recent debate was sparked by the observation of an elastic intensity increase around the quasi-commensurate wavevector $Q \sim (0.33, 0)$. This was first interpreted as evidence of charge order analogous to the Charge Density Waves observed in cuprates[49,50,57], but later dismissed as resulting from the periodic arrangement of residual apical oxygens from incomplete topotactic reduction[58,59]. Our integrals of the spectral weight in the quasielastic region, displayed in Fig. S1 of the Supplementary Material, show no evidence of such an increase, confirming the absence of charge order in our samples and the fully occurred topotactic reaction.

In order to determine the energy of the magnetic excitations, we fitted the elastic and phonon peaks with resolution-limited Gaussian functions, and the magnetic peak with the damped harmonic oscillator spectral shape, convolved with a Gaussian accounting for the experimental resolution[54] (see Fig. 2a, b). A phonon peak at ≈80 meV was included in the spectral fitting. Phonon and magnon overtones were considered only in the cuprate fit, since in the nickelate, these features are too broad and too close in energy to be reliably disentangled. A similar fit was performed on the high-energy peaks related to the orbital transitions between 3*d* levels (Panels (c, d)), to be discussed in the following. More details about the fittings are available in the Supplementary Information. The momentum-energy dispersions for PNO and CCO are reported in Fig. 3a, while 3b shows a comparison between the extracted damping coefficients, related to the spectral broadening of the magnon, and the corresponding values for superconducting $(Bi,Pb)_2(Sr,La)_2CuO_{6+\delta}$ (Bi2201) samples at different doping levels, taken from ref. 54. The peak broadening for the nickelate is found to be nearly constant (~100 meV) over the explored momentum range. Such a value is obviously larger than for CCO, where the magnetic peak is resolution-limited: in this case, long-range AFM order provides almost undamped spin wave propagation. At the same time, it is less than half the corresponding value for the lowest doping level of superconducting Bi2201 ($\gtrsim$200 meV, within the confidence intervals). This demonstrates that self-doping has a much milder impact on spin order than chemical doping, endowing IL nickelates with a non-disruptive way to achieve superconductivity, which is totally absent in copper oxides.

We also notice an increase in the elastic intensity around the X point, a result previously reported but not discussed, for PNO and $NdNiO_2$[12,52]. Upon approaching the X point in (0.5,0), the spin excitation becomes less intense, and its shape is not an individual peak directly identified with a single magnon, as a consequence of fractionalization phenomena, related to the square lattice and independent of the material[60], and of multi-magnon excitations[61]. At the same time, a continuum, possibly due to spinon pairs, appears and becomes increasingly intense towards the X point: for CCO, these effects are very evident and were previously discussed by Martinelli et al.[55]. For PNO and other IL nickelates, the broadening is harder to determine, but the loss of intensity was previously observed[52]. We consider that here a single-peak fit is accurate enough for our purpose, although for CCO it results in an overestimation of the single-magnon damping energy close to (0.5,0) as shown in Fig. 3a.

To analyze the differences between the two samples, we fitted the extracted dispersion curves with those predicted by Linear Spin Wave (LSW) theory[62], as implemented in the SpinW library in Matlab[63]. We included four in-plane exchange couplings J_{1-4} and one out-of-plane term $J_\perp$, following the strategy previously adopted for CCO in ref. 53. This is new for IL nickelates, whose magnon dispersion has so far been modeled using purely two-dimensional LSW approaches [12,47,52,64] or, at most, by introducing an out-of-plane magnetic anisotropy[65], which is, however, difficult to constrain from RIXS spectra. As for CCO, exchange couplings up to fourth nearest neighbors were needed to reproduce the zone-boundary energy. The inclusion of $J_\perp$ is motivated by the fact that, upon approaching Γ at non-integer L, the single-magnon energy remains large, closely resembling the behavior found in CCO. For PNO, the $J_\perp$ value was not directly estimated as a fitting parameter but was kept fixed during the procedure. The reason lies in the difficulty to safely estimate the value of the gap at the Γ point (see Supplementary Material for more details, in particular Figs. S4 and S8). The value 5.9 meV reported in the figure provided the best fitting quality. Nevertheless, we can reasonably assume $J_\perp$ for PNO to be between 0 and 10 meV. The values of the extracted exchange Js (in meV) are reported in Fig. 3a. The nearest-neighbor exchange J_1 is about twice as large in CCO (82 meV) as in PNO (46 meV), in agreement with the literature[12,24,51]. Conversely, $J_\perp$ is comparable in the two compounds (7 meV for CCO and 6 meV for PNO), leading to an out-to-in-plane exchange ratio $J_\perp/J_1$ of 8.5% for CCO and 13% for PNO. We notice that these values of $J_\perp$ are close to the intra-unit-cell coupling of bilayer cuprates like YBCO[53]. The absence of apical oxygens in IL nickelates leads to a long-range, in-plane hopping phenomenon qualitatively similar to cuprates', despite the larger Δ. We observe that the 3D character of the spin-spin correlation is also similar in the IL nickelates and in the CCO, as testified by the comparable value of the spin excitation energy at the in-plane zone center and non-integer L (60–80 meV, respectively). Whether rare-earth ions play a substantial role in this mechanism, as proposed in several (mainly theoretical) studies[24,66,67], remains unclear, since other works suggest a much weaker influence[17]. Moreover, our results give proof of the fully occurred topotactic reduction of the PNO samples and the absence of interstitial oxygen atoms.

A possible role of epitaxial strain can also be considered, since the two films experience opposite strain conditions: PNO is grown on $SrTiO_3$ (a_{STO} = 3.905 Å), whose lattice parameter is smaller than that of PNO (a_{PNO} = 3.94 Å), whereas CCO is grown on $NdGaO_3$ (a_{NGO} = 3.861 Å), whose lattice parameter is only slightly larger than that of CCO (a_{CCO} = 3.856 Å). This results in a compressive strain of about +0.9% for PNO and a very small tensile strain of about −0.1% for CCO. Epitaxial strain has been shown to affect the in-plane magnetic exchange in both cuprates[68,69] and non-infinite-layer nickelates[65,70,71], with compressive (tensile) strain generally reducing (enhancing) the exchange interaction. In our samples, however, strain would tend to increase J_1 in PNO and slightly reduce it in CCO, thereby opposing the observed difference rather than causing it. Since the strain mismatch is also too small to account for the sizable difference in the extracted exchange values, the smaller J_1 of PNO relative to CCO must be intrinsic.

Along the [H, H] direction, we notice that the maximum of the dispersion in PNO is not at the BZ boundary (0.25,0.25) r.l.u., but rather at (0.2,0.2) r.l.u., and that the elastic peak intensity increases very much beyond the BZ boundary in (0.25,0.25) r.l.u. (see Fig. 1e). These facts might suggest the presence of an incommensurate resonant diffraction reflection distinct from the AFM (0.5,0.5) point, which cannot be reached in RIXS due to kinematic limitations. Those peculiarities had already been observed but not discussed in ref. 52 for PNO and $LaNiO_2$.

To gain further insights, we measured RIXS spectra with analysis of the linear polarization of the scattered photons. We chose large momenta in the [H, 0] direction, with both positive and negative values of $H = \pm 0.4$ r.l.u. for PNO and $H = \pm 0.5$ r.l.u. for CCO. For positive H values, we took both σ and π incident polarization; for negative H, only the σ polarization was used because cross-sections for π incidence are much smaller[46]. The results are shown in Fig. 4, where the spectral components with scattered polarization orthogonal to the incident one ($\sigma\pi'$ and $\pi\sigma'$, i.e., crossed polarization) are given in red and those with parallel polarization ($\sigma\sigma'$ and $\pi\pi'$) are in blue. In Fig. 4c–f, we see that the single magnon peak at positive H has crossed character for both samples, in agreement with literature on cuprates[55,72] and with theory[46,73]. With σ-polarized incident light and positive H, the magnetic peak in CCO is purely parallel, consistent with the transfer of an even number of angular-momentum units (bimagnon). In contrast, in the nickelate, this feature—if present—is too weak and broad to be clearly distinguished (Panels (e) and (b), respectively). In all PNO spectra, we see that an unpolarized continuum is present, likely resulting from self-doping, which leads to a not purely crossed polarization character of the magnon in panel (c) and non-purely parallel polarization of the phonon peak in all spectra.

The differences between the two samples are more evident in the *dd*s spectral region (1–3 eV). Here, the peaks have been fitted as already shown in Fig. 2c, d, and assigned according to the known crystal field splitting of 3*d* orbitals in a square tetragonal environment[46]. Disregarding the peak at 0.7 eV in PNO, the lowest energy feature can be assigned to the d_{xy} orbital excitation in both samples. The energy position obtained by a multi-peak fitting is 1.29 and 1.65 eV for PNO and CCO, respectively, with the difference likely being due to the different hopping parameters and in-plane lattice constants of the two materials, which are also grown on different substrates. The $d_{xz/yz}$ excitation in the cuprate appears split into two components; again, this phenomenon has already been observed[45] but not explained in CCO, although it might not be due to simple splitting between the single d_{xz} and d_{yz} features (see also the comparison with cross-sections explained below). Nevertheless, the $d_{xz/yz}$ energy position is quite similar between the two systems (1.93 eV for PNO, 2.05 eV for the center of mass of the two features of CCO). The d_{z^2} feature in the nickelate is very broad and weak, so that its position is quite hard to estimate precisely. Although determining its exact position is not crucial for our purposes, fitting results suggest it is found at slightly larger energy than in the cuprate. Polarization analysis shows that the $d_{xz/yz}$ features have similar character for PNO and CCO in all three geometries, while the d_{xy} peak is similar at negative H but is very different at positive H. In fact, for $H > 0$ it has a predominant crossed character for π and parallel character for σ for CCO, but it is of mixed polarization character for PNO, at odds with the completely crossed polarization expected from theory (see Fig. 4i). A possible intuitive explanation is the proximity of the 0.7 eV peak, which is fully unpolarized in all cases. The fact that its influence appears maximum in the case of grazing emission and π incidence, where we report the discrepancy, appears consistent with the out-of-plane nature of the peak, already observed in previous studies[50]. Accepting the interpretation of the latter in terms of Ni 3*d*-rare-earth 5*d* hybridized states[11], the mixed polarization character of the 1.29 eV peak might be a hint of stronger hybridization of Pr 5*d* with Ni $3d_{xy}$ states than with the $3d_{xz/yz}$ ones. However, recent photoemission measurements[37] have shown no evidence of rare-earth states close to the Fermi level, highlighting instead a predominating role of electride-like interstitial *s* states, where electrons are delocalized over several voids and coexist with the Ni $3d_{x^2-y^2}$ electrons. It is not excluded that such *s* states can also interact with

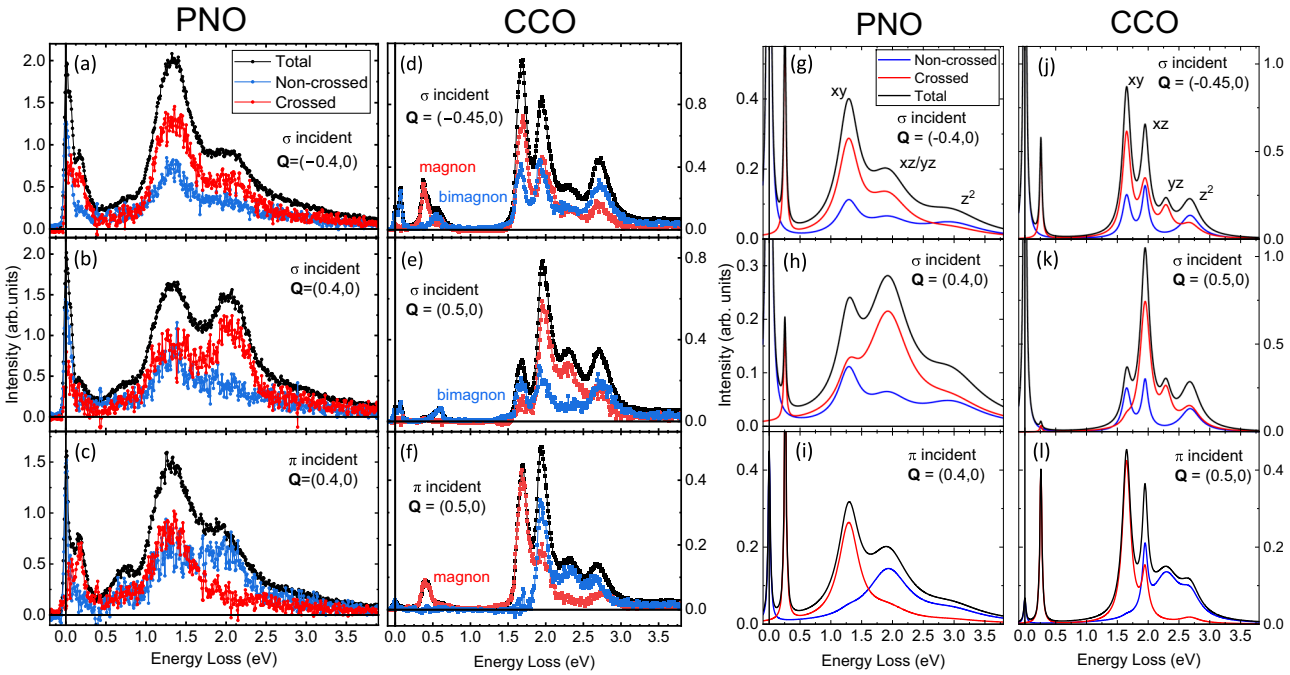


Fig. 4 | Comparison between polarimetric RIXS data and theory. Polarization-resolved RIXS spectra for PNO (**a**–**c**) and CCO (**d**–**f**), measured under the geometry and polarization conditions specified in each panel. **g**–**l** Corresponding single-ion RIXS cross-section calculations for the same polarization and geometry conditions as in (**a**–**f**), respectively.

the $3d_{xy}$ states, which are oriented in the same plane as the $3d_{x^2-y^2}$: further investigation is required to verify this hypothesis. By comparing polarimetric RIXS data with single-ion cross-sections calculations shown in panels (g–l), and based on the energies listed in Table 1, almost all of the CCO spectra can be quite well reproduced. We added here a splitting of the $d_{xz/yz}$ peak into the two separate d_{xz} and d_{yz} features, giving good agreement except for the grazing incidence case. On the other hand, for the PNO spectra, the measured d_{xy} peak at $H = 0.4$ for σ-polarized incident light appears significantly stronger than predicted by the calculations, which may indicate contributions from Pr 5*d* and/or interstitial *s* states.

We conclude the comparison between the orbital excitations by examining their dispersion. If they had a perfectly local nature, they would show no momentum dependence, and in most layered cuprates, this is indeed what has been observed[46,72,74]. For 1D cuprates, it was theoretically proposed and experimentally measured[75,76] that some dispersion can be attributed to an effective orbital exchange interaction (Kugel-Khomskii spin-orbital model)[77], ultimately ascribed to the Cu-O hopping and to 1D fractionalization, which allows orbitons to propagate independently from magnetic excitations[78]. In 2D cuprates, it has been shown theoretically that the mechanism is strongly frustrated by the antiferromagnetic spin order that would immediately dress the propagating orbital excitation with a trail of spin excitations[78,79]. Such coupling between the magnetic and orbital degrees of freedom, which strongly hinders orbiton propagation by nearest neighbor (NN) orbital superexchange, is known as the magnetic string effect and is well-known from the propagation of holes in antiferromagnets[80,81]. However, in CCO the dispersion of the d_{xy} state was recently observed: it is attributed to the large next-nearest neighbor (NNN) orbital superexchange, which allows the orbiton to propagate along the diagonal avoiding coupling to magnons[45]. In Fig. 5a, b, we show that in PNO the d_{xy} peak disperses as a function of momentum. In comparison with the CCO case (c, d), the dispersion has a similar bandwidth but a different shape: the energy is maximal (minimal) at Γ and decreases (increases) with momentum along both the $[H, 0]$ and $[H, H]$ directions for PNO (CCO). To further elucidate the processes underlying the observed orbiton motion, we fit the experimentally observed d_{xy} orbital dispersion in the two materials: the obtained fittings are shown as solid lines in Fig. 5a–c. For PNO, we use the following a priori rather generic and unbiased dispersion relation:

$$\varepsilon_{\boldsymbol{k}} = \varepsilon_{\boldsymbol{0}} + 2t_1^{orb}[\cos(2\pi k_x) + \cos(2\pi ky)] + 2t_2^{orb}[\cos(2\pi k_x)\cos(2\pi ky)] + 2t_3^{orb}[\cos(4\pi k_x) + cos(4\pi k_y)], \quad (1)$$

where t_1^{orb} is the nearest-neighbor (NN) orbiton hopping, t_2^{orb} is the next-nearest-neighbor (NNN) orbiton hopping, and t_3^{orb} is the third-neighbor orbiton hopping. Then, the fitted values of the effective orbiton hoppings are $t_1^{orb} = 12.5 \pm 3.8$ meV, $t_2^{orb} = 0.2 \pm 4.8$ meV, $t_3^{orb} = 5.4 \pm 1.7$ meV, indicating that the dominant orbiton hopping occurs between nearest neighbors.

On the other hand, the orbital dispersion for CCO has already been observed and thoroughly explained[45] by proposing a dominant role of the NNN orbital exchange, following the strong covalence in CCO and suppression of the NN exchange caused by coupling to magnons. Here we follow this interpretation by fitting the CCO orbiton dispersion with the relation

$$\varepsilon_{\boldsymbol{k}} = 2t_2^{orb}\cos(2\pi k_x)\cos(2\pi k_y) \quad (2)$$

retrieving for CCO a next-nearest neighbor hopping $t_2^{orb} = -13.6 \pm 3.5$ meV.

Before attempting to understand the obtained results using a microscopic model, let us stress the big difference between the observed orbiton dispersion in the nickelate and in the cuprate. Whereas in the latter case the (negative) dominant orbital exchange occurs on the same antiferromagnetic sublattice, in PNO the nearest-neighbor hopping is both positive and dominant. This suggests that the origin of the orbiton dispersion in CCO and PNO must be quite different, as explained in detail in the two steps below.

First, the much weaker covalence in PNO than in CCO[6] implies that longer-range orbital superexchange interactions are significantly reduced. Therefore, we expect that, unlike in CCO, the nearest-neighbor orbital

superexchange in PNO strongly dominates over the much weaker next-nearest-neighbor contribution.

To validate this hypothesis, we estimated the NN and NNN orbital superexchange couplings, J^{orb}, in PNO using a simple Hubbard-based three-band model, similar to that previously employed to estimate the orbital superexchange interactions in CCO[45]. Details of this model can be found in the Supplementary Information of ref. 45. The corresponding model parameters are listed in Table 2, where the values for CCO are included for comparison.

The choice of model parameters is crucial in this context, as we discuss them in some detail in the "Methods" section. In the end, by plugging such values from the three-band model into the orbital superexchange formulas given in ref. 45, we find that the NN orbital superexchange is dominant in PNO, while the NNN exchange is relatively small and can be safely neglected below; see Table 3. This is in stark contrast to CCO, where the NNN superexchange was found to be very large and was therefore the only exchange interaction included in the theoretical description[45]. The origin of this difference between the two materials lies in the substantially stronger covalence in the cuprates as compared to the nickelates[6].

Second, having estimated the values of the orbital superexchange couplings in PNO, we are now left with the task of relating these results to the observed orbiton dispersion relations. Here, the first point to stress is that a large nearest-neighbor orbital superexchange drives nearest-neighbor orbiton motion, which is, as discussed above, strongly frustrated in antiferromagnets due to the spin-string effect. In other words, a large nearest-neighbor orbital exchange J_1^{orb} does not automatically imply a large free-orbiton hopping amplitude t_1^{orb}. Indeed, the latter can be strongly suppressed by the string effect, i.e., by the strong scattering of the orbiton off magnons generated during its motion through the antiferromagnetic background.

Nevertheless, it turns out that there exists a "way out," and the effective orbiton hopping is actually quite large in PNO. The key point is that a finite Hund's exchange in the intermediate state of the orbital exchange process allows for a concomitant orbital and spin flip, which leads to a finite orbiton hopping that preserves the antiferromagnetic order. While one might expect such processes to be strongly suppressed, a relatively large ratio of the Hund's exchange J_H to the Hubbard U in PNO makes these processes remarkably efficient. Altogether, this leads to $t_1^{orb} \approx 0.6 J_1^{orb}$ in PNO; see the SM section for more details. Note that the orbiton motion is quite different in CCO[45]. Here the orbiton can move efficiently via a large $t_2^{orb} \approx J_2^{orb}$, as shown in ref. 45.

Finally, in Table 3 we compare the obtained theoretical values of the dominant orbiton hoppings with those extracted from fitting the orbital dispersion (1). We find relatively good agreement between theory and experiment, supporting the scenario discussed above. As a closing remark, we notice that in PNO also the third nearest-neighbor t_3 likely plays an important role in the orbiton propagation, as its extracted value is almost half of t_1. In the above discussion, we did not include t_3, as doing so would require going beyond the approximation used in the SM to solve the model. This constitutes a complex many-body problem that is beyond the scope of the present article. Nevertheless, the investigation of longer-range orbiton propagation dynamics is the next step in the refinement process of the model.

Table 1 | Orbital peak energies (in eV) for PNO and CCO

Orbital peak (eV)	PNO	CCO
d_{xy}	1.29 ± 0.02	1.65 ± 0.02
$d_{xz/yz}$	1.93 ± 0.06	1.95 ± 0.01
		2.29 ± 0.06
d_{z^2}	2.96 ± 0.58	2.68 ± 0.04

Energy losses of the *dd* peaks at the BZ edge as extracted from the fittings in Fig. 2c, d.

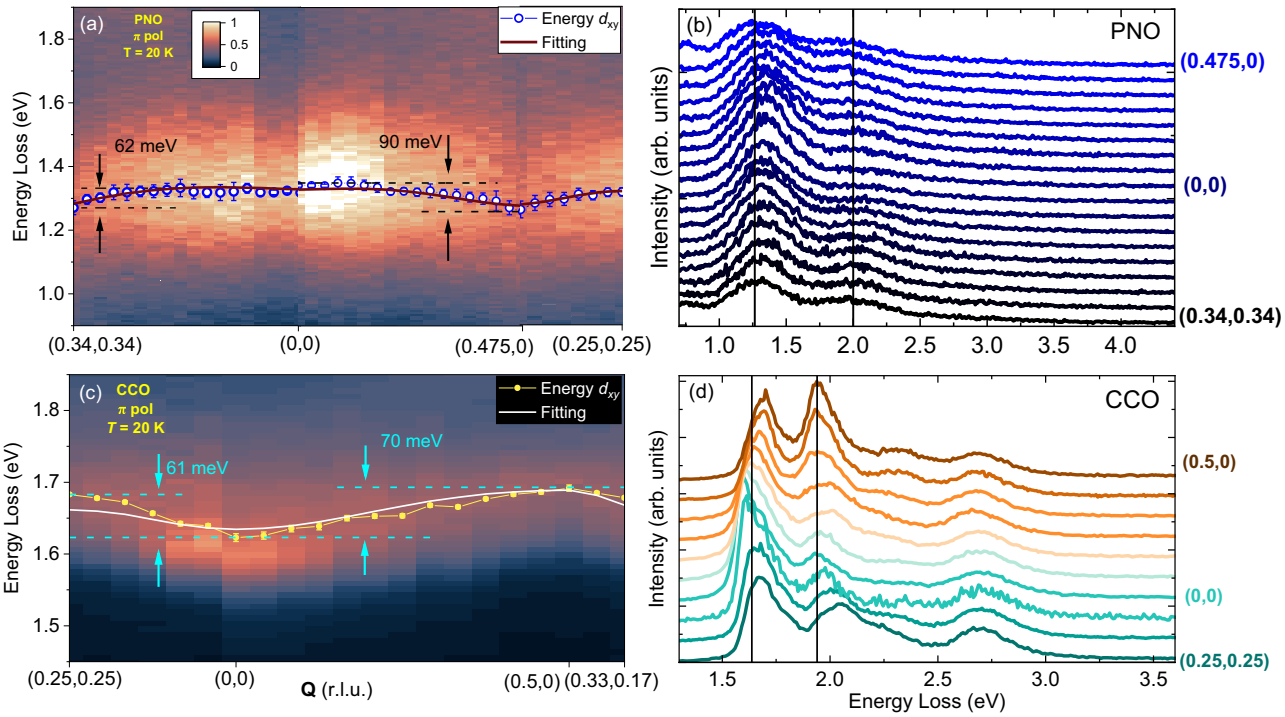


Fig. 5 | Orbital excitation dispersion. a Momentum-resolved map in the d_{xy} energy range of PNO; dots highlight the dispersion of the peak, while the continuous line represents the charge transfer model fitting (see text). Horizontal dashed lines quote the maximum and minimum energies of each branch, with their distance being reported. The followed BZ cuts are the same shown in the inset of Fig. 1d. **b** Stack of spectra of PNO in the whole *dd* range, with vertical lines fixed at the minimum of the dispersion of the d_{xy} and $d_{xz/yz}$ peak. **c**, **d** Same as (**a**, **b**), for CCO. Error bars in (**a**–**c**) represent 95% confidence intervals from the fittings.

Table 2 | Microscopic parameters

Parameter (eV)	PNO	CCO
$t_{pd\sigma}$	1.04	1.30
$t_{pd\pi}$	0.56	0.70
t_{pp}	0.56	0.70
Δ	4.4	1.80
$\epsilon_{\pi\sigma}$	−1.00	−1.60
ϵ_{xy}	0.70	1.00
U	6.5	8.00
J_H	1.2	1.00

Charge transfer model parameters (in eV) employed for the calculation of J_1^{orb} and J_2^{orb} (see text for the model details).

Table 3 | Orbital superexchange and orbiton hopping values

J^{orb}, t^{orb} (meV)	PNO	CCO
Experiment t_1^{orb}	12.5 ± 3.8	-
Experiment t_2^{orb}	0.2 ± 4.8	−13.6 ± 3.5
Theory J_1^{orb}	21.6	-
Theory J_2^{orb}	−0.3	−15.0
Theory t_1^{orb}	13.7	-
Theory t_2^{orb}	~0	−15

Calculated values of the nearest- and next-nearest-neighbor orbital superexchange J^{orb} (in meV) for PNO and CCO, together with the corresponding effective orbiton hopping amplitudes t^{orb} (in meV), compared to those extracted from fits to the data in Fig. 5a–c; see text for further details.

To summarize, our comparative study of the spin, charge and orbital excitations in IL nickelates and cuprates uncovers key similarities and distinctions that shed new light on their correlated electronic states. In IL nickelates, in-plane hopping integrals are smaller than in cuprates, leading to approximately half the nearest neighbor exchange interaction and to a substantially lower energy of the d_{xy} excitation. However, in both families, the absence of apical oxygens causes significant long-range hopping integrals that shape the magnon in-plane dispersion and give rise to dispersing orbital excitations. The inter-plane direct exchange interaction seems little affected by the presence of a rare-earth, as in IL nickelates or of an alkali metal ion, as in cuprates. In both cases, the out-of-plane coupling generates 3D antiferromagnetic correlations in the IL compounds. The rare-earth in the nickelates leads to a more tridimensional electronic structure and to self-doping effects resulting in a charge continuum that merges with *dd* excitations in RIXS spectra. The orbital dispersion in the IL nickelate seems to primarily involve nearest-neighbor orbital superexchange interaction, which in cuprates is strongly hampered by coupling to magnons. Combining these observations, we can speculate that IL nickelates are indeed mimicking the essential physics of cuprates, including the mechanisms for superconducting pairing. The lower T_c in IL nickelates is mainly due to the overall smaller energy of spin fluctuations, which can be traced back to larger charge transfer Δ and/or smaller hopping integrals. In addition, the Mott-Hubbard nature of the correlation in IL nickelates, which causes a stronger localization of the doping charge on the metal site, might also imply a smaller electron-phonon interaction and the lack of charge density waves and fluctuations ubiquitous in hole-doped cuprates.

In conclusion, infinite-layer nickelates appear to share many key properties with cuprates, although with reduced interaction energies. We can safely state that the exchange interaction between different planes clearly confers a certain degree of tridimensionality to the magnetism of PNO, notwithstanding the difficulty in exactly quantifying this effect through the size of the gap at Γ. At the same time, the presence of the rare-earth ion enables a doping mechanism that is absent in infinite-layer cuprates because of the lack of apical oxygens. Together, these observations indicate that infinite-layer nickelates are unconventional superconductors closely related to cuprates, but lacking some of the ingredients that enhance T_c in the latter.

Methods

Pristine perovskite $PrNiO_3$ thin films were grown by RHEED-monitored Pulsed Laser Deposition on a $SrTiO_3$ (001) substrate (STO), up to a thickness of 15–20 unit cells (~5 nm), and capped with an epitaxial STO layer grown in situ up to 12 unit cells (~3 nm). Superconductive IL phase $PrNiO_2$ was then obtained via a topotactic chemical reduction, consisting of the deintercalation of apical oxygen atoms by means of a high-T annealing in a hydrogen-rich atmosphere issued from a CaH_2 powder, as done in previous studies[82–86]. The resulting samples show a complete superconducting behavior below T_c = 4 K, while the SC onset (maximum curvature in the resistivity $\rho(T)$) is located slightly below 11 K. The lattice parameters for the IL phase were found to be a = 3.94 Å and c = 3.28 Å. More details about sample growth and characterization are available in ref. 42. The CCO presented data are a re-analysis of the same raw dataset already partly published in Refs. 45,55. The CCO films were grown by pulsed-laser deposition (KrF excimer laser, λ = 248 nm) at a temperature around 600 °C and an oxygen pressure of 0.1 mbar, on $NdGaO_3$ (NGO) (110) substrate. The substrate holder was at a distance of 2.5 cm from the CCO target, which was prepared by a standard solid-state reaction[43,44]. The lattice constants for CCO, as determined from XRD, are $a = b$ = 3.863 Å and c = 3.184 Å. The measured resistivity of CCO at room temperature (300 K) was ~10^4 mΩ cm. Below 250 K, the film resistance exceeded the upper limit of our measurement setup[45].

RIXS measurements were performed with the ERIXS spectrometer at the ID32 beamline of the European Synchrotron (ESRF), in Grenoble[87]. The beamline and spectrometer combined resolution was 40 meV at the Ni L_3 edge (852.4 eV) of PNO and 42 meV at the Cu L_3 edge (930.6 eV) of CCO. We measured momentum-resolved RIXS maps on both materials along the $M - \Gamma - X - M$ cuts of the BZ; for PNO, the Ni-L_3 resonance energy is actually not enough to reach the X point, so we stopped at $\mathbf{Q} = (0.475, 0)$ (see the inset of Fig. 1d). We used π linear incident polarization and near grazing emission geometry (positive values of H) to enhance the spin non-conserving cross-section versus the spin-conserving ones[73,88,89]. Selected spectra were taken with polarization resolution of the scattered photons[72,87,90]. In this case, we employed both grazing incidence (θ = 24° as measured from the sample surface) and grazing emission (θ = 125°) geometry, both with π and σ incident polarizations. All data were collected at T = 20 K with a fixed scattering angle 2θ = 149. 5°; therefore, the value of the out-of-plane momentum component L was not fixed when scanning the in-plane components H and K. This is not an issue, since the in-plane exchange Js are still dominating the out-of-plane $J_\perp$.

All fittings were carried out with the software MATLAB. The library SpinW[63] was used for the extraction of the exchange couplings J_x from the magnetic dispersion relations. For the orbital dispersion, calculation of theoretical J_1^{orb} and J_2^{orb} was based on the same charge transfer model reported in the Supplementary Information of ref. 45.

Concerning the parameter choice for the orbiton propagation model, for PNO, the hopping integrals were reduced to 80% of their corresponding CCO values, to account for the larger d-p energy splitting[6]. The splittings $\epsilon_{\pi\sigma}$ and ϵ_{xy} values were taken from electronic structure calculations[6]. The value of Hund's exchange was estimated based on the atomic value for the nickel ion[91], assuming a significantly smaller reduction in the solid state than that typically observed in cuprates. This is attributed to the reduced nephelauxetic effect (orbital cloud expansion)[92] in nickelates, where lower covalence preserves the intra-atomic nature of the exchange interaction more effectively than in the highly covalent cuprates.

Since there is no clear consensus in the literature on the values of the charge-transfer energy Δ and the Mott interaction U, we adopted Δ from DFT calculations[6], while U was taken from values proposed for the tri-layer nickelate $La_4Ni_3O_8$[29]. Although the Ni valence in that compound is not identical to that of the infinite-layer nickelates, this choice is consistent with

the mixed Mott-Hubbard/charge-transfer regime proposed as a common framework for the nickelate family[30]. The Δ value has also been very recently corroborated by photoemission measurements on the $n = 8$ nickelate $Nd_9Ni_8O_{18}$[93].

Data availability

All data shown in the main text and in the Supplementary Information are available at the Zenodo repository at Spin and orbital excitations in undoped infinite-layer superconducting PrNiO2 and insulating CaCuO2 | Zenodo.

Received: 21 October 2025; Accepted: 29 June 2026;
Published online: 21 July 2026

References

1. Fradkin, E., Kivelson, S. A. & Tranquada, J. M. Colloquium: theory of intertwined orders in high temperature superconductors. *Rev. Mod. Phys.* **87**, 457–482 (2015).
2. Keimer, B., Kivelson, S. A., Norman, M. R., Uchida, S. & Zaanen, J. From quantum matter to high-temperature superconductivity in copper oxides. *Nature* **518**, 179–186 (2015).
3. Zaanen, J. & Sawatzky, G. Systematics in band gaps and optical spectra of 3D transition metal compounds. *J. Solid State Chem.* **88**, 8–27 (1990).
4. Botana, A. S., Lee, K.-W., Norman, M. R., Pardo, V. & Pickett, W. E. Low valence nickelates: launching the nickel age of superconductivity. *Front. Phys.* **9**, 813532 (2022).
5. Kitatani, M. et al. Nickelate superconductors—a renaissance of the one-band Hubbard model. *npj Quantum Mater.* **5**, 59 (2020).
6. Botana, A. S. & Norman, M. R. Similarities and differences between $LaNiO_2$ and $CaCuO_2$ and implications for superconductivity. *Phys. Rev. X* **10**, 011024 (2020).
7. Nomura, Y. & Arita, R. Superconductivity in infinite-layer nickelates. *Rep. Prog. Phys.* **85**, 052501 (2022).
8. Jiang, P., Si, L., Liao, Z. & Zhong, Z. Electronic structure of rare-earth Infinite-Layer $RNiO_2$(R = La,Nd). *Phys. Rev. B* **100**, 201106 (2019).
9. Goodge, B. H. et al. Doping evolution of the Mott–Hubbard landscape in Infinite-Layer Nickelates. *Proc. Natl. Acad. Sci. USA*. **118**, e2007683118 (2021).
10. Zeng, S. et al. Phase diagram and Superconducting dome of Infinite-Layer $Nd_{1-x}Sr_xNiO_2$ Thin Films. *Phys. Rev. Lett.* **125**, 147003 (2020).
11. Hepting, M. et al. Electronic structure of the parent compound of superconducting infinite-layer nickelates. *Nat. Mater.* **19**, 381–385 (2020).
12. Lu, H. et al. Magnetic excitations in infinite-layer nickelates. *Science* **373**, 213–216 (2021).
13. Ortiz, R. A. et al. Magnetic correlations in infinite-layer nickelates: an experimental and theoretical multimethod study. *Phys. Rev. Res.* **4**, 023093 (2022).
14. Li, D. et al. Superconductivity in an infinite-layer nickelate. *Nature* **572**, 624–627 (2019).
15. Zeng, S. et al. Superconductivity in infinite-layer nickelate $La_{1-x}Ca_xNiO_2$ thin films. *Sc. Adv.* **8**, eabl9927 (2022).
16. Chow, S., Luo, Z. & Ariando, A. Bulk superconductivity near 40 K in hole-doped $SmNiO_2$ at ambient pressure. *Nature* **642**, 58–63 (2025).
17. Osada, M. et al. Nickelate Superconductivity without rare-earth magnetism: (La,Sr)NiO_2. *Adv. Mater.* **33**, 2104083 (2021).
18. Osada, M. et al. A superconducting praseodymium nickelate with infinite layer structure. *Nano Lett.* **20**, 5735–5740 (2020).
19. Zeng et al. Origin of local magnetic exchange interaction in infinite-layer nickelates. APS Global Physics Summit 2026. American Physical Society https://summit.aps.org/smt/2026/events/MAR-J31/3 (2026).
20. DahabDahab, H. et al. Unveiling the key role of rare-earth (La versus Nd) in Ni^+-based layered nickelates: impact on structures and physical properties. *Chem. Mater.* **37**, 7671–7686 (2025).
21. Rossi, M. et al. Orbital and spin character of doped carriers in infinite-layer nickelates. *Phys. Rev. B* **104**, L220505 (2021).
22. Krieger, G. et al. Signatures of canted antiferromagnetism in infinite-layer nickelates studied by X-ray magnetic dichroism. *Phys. Rev. B* **110**, 195110 (2024).
23. Lee, K.-W. & Pickett, W. Infinite-layer $LaNiO_2$: Ni^{1+} is not Cu^{2+}. *Phys. Rev. B* **70**, 165109 (2004).
24. Been, E. et al. Electronic structure trends across the rare-earth series in superconducting infinite-layer nickelates. *Phys. Rev. X* **11**, 011050 (2021).
25. Worm, P. et al. Correlations tune the electronic structure of pentalayer nickelates into the superconducting regime. *Phys. Rev. Mater.* **6**, L091801 (2022).
26. Zaanen, J., Sawatzky, G. & Allen, J. Band gaps and electronic structure of transition-metal compounds. *Phys. Rev. Lett.* **55**, 418 (1985).
27. Chen, Z. et al. Electronic structure of superconducting nickelates probed by resonant photoemission spectroscopy. *Matter* **5**, 1806–1815 (2022).
28. Lin, J. et al. Strong superexchange in a $9-\delta$ Nickelate revealed by resonant inelastic X-ray scattering. *Phys. Rev. Lett.* **126**, 087001 (2021).
29. Shen, Y. et al. Role of oxygen states in the low-valence nickelate $La_4Ni_3O_8$. *Phys. Rev. X* **12**, 011055 (2022).
30. Shen, Y. et al. Electronic character of charge order in square-planar low-valence nickelates. *Phys. Rev. X* **13**, 011021 (2023).
31. Weihe, H., Güdel, H. U. & Toftlund, H. Superexchange in magnetic insulators: an interpretation of the metal-metal charge transfer energy in the Anderson theory. *Inorg. Chem.* **39**, 1351–1362 (2000).
32. Kapeghian, J. & Botana, A. S. Electronic structure and magnetism in infinite-layer nickelates $RNiO_2$ (R = La-Lu). *Phys. Rev. B* **102**, 205130 (2020).
33. Yang, Y.-f. & Zhang, G.-M. Self-doping and the Mott-Kondo scenario for infinite-layer nickelate superconductors. *Front. Phys.* **9**, 801236 (2022).
34. Zhang, G.-M., Yang, Y.-f. & Zhang, F.-C. Self-doped Mott insulator for parent compounds of nickelate superconductors. *Phys. Rev. B* **101**, 020501 (2020).
35. Lechermann, F. Late transition metal oxides with infinite-layer structure: nickelates versus cuprates. *Phys. Rev. B* **101**, 081110 (2020).
36. Ding, X. et al. Cuprate-like electronic structures in infinite-layer nickelates with substantial hole dopings. *Nat. Sc. Rev.* **11**, nwae194 (2024).
37. Li, C. et al. Observation of electridelike *s* states coexisting with correlated *d* electrons in $NdNiO_2$. *Phys. Rev. Lett.* **135**, 116501 (2025).
38. Worm, P. et al. Spin fluctuations sufficient to mediate superconductivity in nickelates. *Phys. Rev. B* **109**, 235126 (2024).
39. Scalapino, D. J. A common thread: the pairing interaction for unconventional superconductors. *Rev. Mod. Phys.* **84**, 1383–1417 (2012).
40. Saykin, D. R. et al. Spin-glass state in nickelate superconductors. *npj Quantum Mater.* **10**, 94 (2025).
41. Fowlie, J. et al. Intrinsic magnetism in superconducting infinite-layer nickelates. *Nat. Phys.* **18**, 1043–1047 (2022).
42. Sahib, H. et al. Superconductivity in $PrNiO_2$ infinite-layer nickelates. *Adv. Mater.* **37**, e2416187 (2025).
43. Stellino, E., Postorino, P., Sanna, S., Tebano, A. & Di Castro, D. On the role of strain-and doping-induced disorder in epitaxial $CaCuO_2$ films: lattice and spin dynamics in light scattering response. *J. Appl. Phys.* **137**, https://pubs.aip.org/aip/jap/article/137/18/185301/3346601 (2025).
44. Di Castro, D. et al. High-T_c superconductivity at the interface between the $CaCuO_2$ and $SrTiO_3$ insulating oxides. *Phys. Rev. Lett.* **115**, 147001 (2015).

45. Martinelli, L. et al. Collective nature of orbital excitations in layered cuprates in the absence of apical oxygens. *Phys. Rev. Lett.* **132**, 066004 (2024).
46. Moretti Sala, M. et al. Energy and symmetry of *dd* excitations in undoped layered cuprates measured by Cu L_3 resonant inelastic X-ray scattering. *New J. Phys.* **13**, 043026 (2011).
47. Gao, Q. et al. Magnetic excitations in strained Infinite-Layer nickelate $PrNiO_2$ films. *Nat. Commun.* **15**, 5576 (2024).
48. Hayashida, S. et al. Investigation of spin excitations and charge order in bulk crystals of the infinite-layer nickelate $LaNiO_2$. *Phys. Rev. B* **109**, 235106 (2024).
49. Tam, C. C. et al. Charge density waves in infinite-layer $NdNiO_2$ nickelates. *Nat. Mater.* **21**, 1116–1120 (2022).
50. Krieger, G. et al. Charge and spin order dichotomy in $NdNiO_2$ driven by the capping layer. *Phys. Rev. Lett.* **129**, 27002 (2022).
51. Rosa, F. et al. Spin excitations in $Nd_{1-x}Sr_xNiO_2$ and $YBa_2Cu_3O_{7-\delta}$: the influence of Hubbard *U*. *Phys. Rev. B* **110**, 224431 (2024).
52. Rossi, M. et al. Universal orbital and magnetic structures in infinite-layer nickelates. *Phys. Rev. B* **109**, 024512 (2024).
53. Peng, Y. et al. Influence of apical oxygen on the extent of in-plane exchange interaction in cuprate superconductors. *Nat. Phys.* **13**, 1201–1206 (2017).
54. Peng, Y. et al. Dispersion, damping, and intensity of spin excitations in the monolayer $(Bi,Pb)_2(Sr,La)_2CuO_{6+\delta}$ cuprate superconductor family. *Phys. Rev. B* **98**, 144507 (2018).
55. Martinelli, L. et al. Fractional spin excitations in the infinite-layer cuprate $CaCuO_2$. *Phys. Rev. X* **12**, 021041 (2022).
56. Braicovich, L. et al. Dispersion of magnetic excitations in the cuprate La_2CuO_4 and $CaCuO_2$ compounds measured using resonant X-ray scattering. *Phys. Rev. Lett.* **102**, 167401 (2009).
57. Rossi, M. et al. A broken translational symmetry state in an infinite-Layer nickelate. *Nat. Phys.* **18**, 869–873 (2022).
58. Raji, A. et al. Charge distribution across capped and uncapped infinite-layer neodymium nickelate thin films. *Small* **19**, 2304872 (2023).
59. Parzyck, C. T. et al. Absence of $3a_0$ charge density wave order in the infinite-layer nickelate $NdNiO_2$. *Nat. Mater.* **23**, 486–491 (2024).
60. Dalla Piazza, B. et al. Fractional excitations in the square-lattice quantum antiferromagnet. *Nat. Phys.* **11**, 62–68 (2015).
61. Betto, D. et al. Multiple-Magnon excitations shape the spin spectrum of cuprate parent compounds. *Phys. Rev. B* **103**, L140409 (2021).
62. Coldea, R. et al. Spin waves and electronic interactions in La_2CuO_4. *Phys. Rev. Lett.* **86**, 5377 (2001).
63. SpinW software. https://spinw.org/.
64. Yan et al. Persistent paramagnons in high-temperature infinite-layer nickelate superconductors. *Nature Communications* https://www.nature.com/articles/s41467-026-73083-3 (2026).
65. Biało, I. et al. Strain-tuned incompatible magnetic exchange-interaction in La_2NiO_4. *Commun. Phys.* **7**, 230 (2024).
66. Peng, C., Jiang, H.-C., Moritz, B., Devereaux, T. P. & Jia, C. Charge order and superconductivity in a two-band model for infinite-layer nickelates. *Phys. Rev. B* **108**, 245115 (2023).
67. Zhang, Y., Zhang, J., He, X., Wang, J. & Ghosez, P. Rare-earth control of phase transitions in infinite-layer nickelates. *PNAS Nexus* **2**, pgad108 (2023).
68. Minola, M. et al. Measurement of the effect of lattice strain on Magnetic interactions and orbital splitting in $CaCuO_2$ using resonant inelastic X-ray scattering. *Phys. Rev. B Cond. Matter Mater. Phys.* **87**, 085124 (2013).
69. Ivashko, O. et al. Strain-engineering mott-insulating La_2CuO_4. *Nat. Commun.* **10**, 786 (2019).
70. Chen, X. et al. Electronic and magnetic excitations in $La_3Ni_2O_7$. *Nat. Commun.* **15**, 9597 (2024).
71. Zhong, H. et al. Epitaxial strain tuning of electronic and spin excitations in $La_3Ni_2O_7$ thin films. *arXiv* (2025).
72. Fumagalli, R. et al. Polarization-resolved Cu L_3-edge resonant inelastic X-ray scattering of orbital and spin excitations in $NdBa_2Cu_3O_{7-\delta}$. *Phys. Rev. B* **99**, 134517 (2019).
73. Ament, L. J., Ghiringhelli, G., Sala, M. M., Braicovich, L. & van den Brink, J. Theoretical demonstration of how the dispersion of magnetic excitations in cuprate compounds can be determined using resonant inelastic X-ray scattering. *Phys. Rev. Lett.* **103**, 117003 (2009).
74. Igarashi, J.-I. & Nagao, T. Magnetic excitations in *L*-edge resonant inelastic X-ray scattering from cuprate compounds. *Phys. Rev. B Cond. Matter Mater. Phys.* **85**, 064421 (2012).
75. Schlappa, J. et al. Spin-Orbital separation in the quasi-one-dimensional Mott insulator Sr_2CuO_3. *Nature* **485**, 82–85 (2012).
76. Fumagalli, R. et al. Mobile orbitons in Ca_2CuO_3: crucial role of Hund's exchange. *Phys. Rev. B* **101**, 205117 (2020).
77. Kugel, K. I. & Khomskii, D. The Jahn-Teller effect and magnetism: transition metal compounds. *Sov. Phys. Uspekhi* **25**, 231 (1982).
78. Wohlfeld, K., Daghofer, M., Nishimoto, S., Khaliullin, G. & van den Brink, J. Intrinsic coupling of orbital excitations to spin fluctuations in Mott insulators. *Phys. Rev. Lett.* **107**, 147201 (2011).
79. Wohlfeld, K., Daghofer, M., Khaliullin, G. & van den Brink, J. Dispersion of orbital excitations in 2D quantum antiferromagnets. *J. Phys. Conf. Ser.* **391**, 012168 (2012).
80. Kane, C. L., Lee, P. A. & Read, N. Motion of a single hole in a quantum antiferromagnet. *Phys. Rev. B* **39**, 6880–6897 (1989).
81. Martinez, G. & Horsch, P. Spin polarons in the t-J model. *Phys. Rev. B* **44**, 317–331 (1991).
82. Lee, K. et al. Aspects of the synthesis of thin film superconducting infinite-layer nickelates. *APL Mater.* **8**, https://pubs.aip.org/aip/apm/article/8/4/041107/123058 (2020).
83. Krieger, G. et al. Synthesis of infinite-layer nickelates and influence of the capping-layer on magnetotransport. *J. Phys. D Appl. Phys.* **56**, 024003 (2023).
84. Puphal, P. et al. Synthesis and physical properties of $LaNiO_2$ crystals. *Phys. Rev. Mater.* **7**, 014804 (2023).
85. Hayward, M., Green, M., Rosseinsky, M. & Sloan, J. Sodium hydride as a powerful reducing agent for topotactic oxide deintercalation: synthesis and characterization of the Nickel(I) oxide $LaNiO_2$. *J. Am. Chem. Soc.* **121**, 8843–8854 (1999).
86. Hayward, M. & Rosseinsky, M. Synthesis of the infinite layer Ni(I) phase $NdNiO_{2+x}$ by low temperature reduction of $NdNiO_3$ with sodium hydride. *Solid State Sci.* **5**, 839–850 (2003).
87. Brookes, N. B. et al. The beamline ID32 at the ESRF for soft X-ray high energy resolution resonant inelastic X-ray scattering and polarisation dependent X-ray absorption spectroscopy. *Nucl. Instrum. Methods Phys. Res. Sect. A* **903**, 175–192 (2018).
88. Braicovich, L. et al. Momentum and polarization dependence of single-magnon spectral weight for Cu L_3-edge resonant inelastic X-ray scattering from layered cuprates. *Phys. Rev. B* **81**, 174533 (2010).
89. Haverkort, M. Theory of resonant inelastic X-ray scattering by collective magnetic excitations. *Phys. Rev. Lett.* **105**, 167404 (2010).
90. Braicovich, L. et al. The simultaneous measurement of energy and linear polarization of the scattered radiation in resonant inelastic soft X-ray scattering. *Rev. Sci. Instrum.* **85**, 115104 (2014).
91. Haverkort, M. W. *Spin and Orbital Degrees of Freedom in Transition Metal Oxides and Oxide Thin Films Studied by Soft X-ray Absorption Spectroscopy*. PhD thesis, University of Cologne. https://arxiv.org/abs/cond-mat/0505214 (2005).
92. Schäffer, C. E. & Jørgensen, C. K. The nephelauxetic series of ligands corresponding to increasing tendency of partly covalent bonding. *J. Inorg. Nucl. Chem.* **8**, 143–148 (1958).
93. Scott, K. et al. Contrasting spin excitations in octahedral and square-planar n=8 Ruddlesden-Popper nickelates. Preprint at *arXiv* https://doi.org/10.48550/arXiv.2603.26593 (2026).

Acknowledgements
The authors thank Marco Moretti Sala and Mark Dean for their valuable discussion. This research used ESRF beamline ID32 under the Proposal No. HC5438, using the ERIXS spectrometer designed jointly by the ESRF and Politecnico di Milano.

Author contributions
F.R., G.M., L.M., N.B., M.S. and G.G. conceived and performed the RIXS measurements, with suggestions from R.A. and D.P. H.S. and D.P. grew and characterized the PNO thin films; D.D.C. grew and characterized the CCO films. F.R. analyzed the RIXS experimental data and performed the fittings. F.R., M.S. and G.G. discussed and interpreted the results. K.W. developed the theoretical model for orbiton propagation. M.Z. performed single-ion calculations. F.R. and G.G. wrote the manuscript with major suggestions from R.A. and K.W. and contributions from all authors.

Funding
F.R., G.M., L.M., M.Z., M.S., and G.G. acknowledge support by the projects PRIN2017 Quantum-2D-ID 2017Z8TS5Band PRIN 2020 QT-FLUO ID 20207ZXT4Z of the Ministry for University and Research (MIUR) of Italy. D.P. acknowledges the ANR-FRANCE (French National Research Agency) for its financial support of the T-ERC project ORBIFUN ANR-23-ERCS-0003-01. This work was partially performed within the MUSA-Multilayered Urban Sustainability Action project, funded by the European Union-NextGenerationEU, under the National Recovery and Resilience Plan (NRRP) Mission 4 Component 2 Investment Line 1.5: Strengthening of research structures and creation of R&D, "innovation ecosystems" set up of "territorial leaders" in R&D. K.W. acknowledges the support of National Science Centre in Poland under Project No. 2024/55/B/ST3/03144 and No. 2021/43/B/ST3/02166. The work by G.M. was jointly supported by Politecnico di Milano and European X-ray Free Electron Laser Facility GmbH.

Competing interests
The authors declare no competing interests.

Additional information
Supplementary information The online version contains supplementary material available at https://doi.org/10.1038/s43246-026-01266-y.

Correspondence and requests for materials should be addressed to F. Rosa or G. Ghiringhelli.

Peer review information *Communications Materials* thanks the anonymous reviewers for their contribution to the peer review of this work. A peer review file is available.

Reprints and permissions information is available at http://www.nature.com/reprints

Publisher's note Springer Nature remains neutral with regard to jurisdictional claims in published maps and institutional affiliations.

Open Access This article is licensed under a Creative Commons Attribution-NonCommercial-NoDerivatives 4.0 International License, which permits any non-commercial use, sharing, distribution and reproduction in any medium or format, as long as you give appropriate credit to the original author(s) and the source, provide a link to the Creative Commons licence, and indicate if you modified the licensed material. You do not have permission under this licence to share adapted material derived from this article or parts of it. The images or other third party material in this article are included in the article's Creative Commons licence, unless indicated otherwise in a credit line to the material. If material is not included in the article's Creative Commons licence and your intended use is not permitted by statutory regulation or exceeds the permitted use, you will need to obtain permission directly from the copyright holder. To view a copy of this licence, visit http://creativecommons.org/licenses/by-nc-nd/4.0/.

© The Author(s) 2026